Effect of intense laser irradiation on the thermal transport properties of metals

Pravin Karna and Ashutosh Giri[*]

Department of Mechanical Industrial and Systems Engineering, University of Rhode Island, Kingston, Rhode Island 02881, USA

Ultrafast laser irradiation of metals can elevate the temperature of electrons to the same order as the Fermi temperature while the lattice remains cold. In this transient and highly nonequilibrium regime, the material properties can undergo drastic modifications, revealing insights into the physical phenomena of the condensed state that are otherwise not evident under equilibrium conditions. However, a clear description of these phenomena, even for elemental metals, remains greatly unexplored partly due to the limitations imposed by the phenomenological treatment of electron-phonon scattering with simplified assumptions for these highly nonequilibrium regimes. In this work, using recent advancements in first-principles calculations, we provide a detailed understanding of hot electron dynamics in a free-electron-like metal (aluminum) and a noble metal (gold) to demonstrate the important role played by the electronic structure in dictating their transport properties at elevated electron temperatures. By performing parameter-free density functional theory calculations of the electron-temperature-dependent heat capacities, electron-phonon coupling, electron mean-free paths, and thermal conductivities, we show that semiempirical and free-electron estimations can lead to erroneous predictions, especially for the case of gold where the excitation of the low-lying d bands can drastically modify the transport properties. We find that the diffusive mean-free paths of electrons in gold can be increased from $\sim$35 nm at ambient conditions to $\sim$70 nm at electron temperatures of $k_B T_e = 6$ eV as a result of drastically reduced electron-phonon scattering. In contrast, we find that the mean-free paths of electrons in aluminum are relatively insensitive to high electron temperature perturbations mainly resulting from the unchanged electron-phonon scattering even at elevated electron temperatures. This ultimately results in a much greater increase in the thermal conductivity of gold at electron temperatures of $\sim$20000 K, where it increases by more than two orders of magnitude. However, in aluminum, the thermal conductivity increase at the elevated electron temperatures is relatively not as pronounced (which increases by a factor of $\sim$70). Our results shed light on the microscopic understanding of hot electron dynamics in metals and is crucial for a plethora of applications such as in plasmonic devices.

I. INTRODUCTION

The complete understanding of electron-phonon (e-p) nonequilibrium in metals is not only of significance to various phenomena in materials physics such as superconductivity [1–3], spintronics [4], electrical and thermal transport [5–7], and laser-induced phase transitions [8–11], but it also underpins the progress in a wide array of applications such as in photovoltaics [12–14], plasmonic devices [15–17], nonlinear optics and catalysis [18–21]. As such, a considerable amount of prior work (dating back to Drude's theory on describing the scattering processes of a free electron gas in 1900) [22] has been devoted to understanding the e-p scattering in metals. For instance, time-resolved experiments based on femtosecond laser pulse excitation of various metals have measured their e-p coupling factor (G), which quantifies the volumetric rate of energy transfer between the phononic and electronic subsystems [7,16,23–28]. Immediately after short-pulse laser irradiation, preferential heating of the electron subsystem (as compared to the cooler lattice) can elevate the electron temperature to values comparable to the Fermi energy, creating thermodynamic nonequilibrium

between the two states. Describing the evolution of this highly nonequilibrium regime has been the subject of intense research over the past several decades.

A significant amount of works focusing on understanding e-p interactions in metals have tried to describe the many-body process by utilizing approximate models, such as those based on the free-electron theory. However, these simplified models are only applicable to a limited number of metals that typically do not possess complex electronic band structures. For example, the free-electron theory is mostly applicable to metals with relatively constant density of states (DOS) around the Fermi level [29–31]. Nevertheless, to describe the temporal and spatial evolution of the temperature profiles of phonons and electrons in an array of metals, the simplified models are mostly coupled with the two-temperature model (TTM), that is given as [32],

$$C_e(T_e)\frac{\partial T_e}{\partial t} = \nabla.(\kappa_e \nabla T_e) - G(T_e - T_p) + S(t),$$

$$C_p(T_p)\frac{\partial T_p}{\partial t} = \nabla.(\kappa_p \nabla T_p) + G(T_e - T_p), \quad (1)$$

where T_e and T_p are the electronic and lattice temperatures, respectively, C_e, C_p, κ_e, and κ_p are the heat capacities and thermal conductivities of the electrons and the lattice vibrations, respectively, and $S(t)$ is the source term. This TTM

*ashgiri@uri.edu

formulation has been extensively used to interpret time-resolved experiments based on pump-probe spectroscopies by assuming that the measured G is constant throughout the relaxation process [7,32–35]. Although these experiments are usually carried out at low electron temperature perturbations (less than several thousand Kelvin), the interpretation of a constant G throughout the entire relaxation process (which for a metal with weak e-p coupling, such as that in gold, can last for several picoseconds) has been shown to not be entirely valid [7,15,32,33,36–39]. Therefore, the often used simplification in the TTM, i.e., the treatment of thermophysical parameters, (such as G, C_e, and κ_e) as phenomenological temperature-independent constants, is invalid for conditions of strong nonequilibrium. Moreover, studies that have treated the temperature dependence of some of these physical properties do not directly account for the effect of highly nonequilibrium electron gas perturbations on the time variant ion-electron and ion-ion potentials while calculating the e-p interactions. These variations, as a result of the e-p nonequilibrium, ultimately dictate the thermophysical properties, which have often been assumed to be temperature-independent constants [31,38–40]. For example, by combining density functional theory (DFT)-based electronic structure calculations with an empirical treatment of the e-p interactions in noble and transition metals, Lin *et al.* [38] have shown that $G(T_e)$ can be significantly increased at high electron temperatures from the thermal excitation of the lower-lying d-band electrons. Their calculations, however, neglect the effect of electron perturbation on both the electronic structure and the mass enhancement parameter (λ), both of which can significantly alter the thermophysical properties, as we will show in this work. Therefore, to fully understand the role of e-p interactions in highly nonequilibrium regimes, such as those during and immediately after ultrashort laser irradiation of metals, one must consider the parameter-free DFT calculations of e-p matrix elements by directly accounting for variations in the phonon spectrum as well as changes in the electronic band structure caused by the electron perturbation, which has remained elusive thus far.

Although more rigorous *ab initio* treatments of the e-p coupling based on linear response theory have studied the spectral nature of the Eliashberg function and its influence on electrical resistivity and κ_e [5,41,42], these calculations, however, were carried out over coarse electron (**k**) and phonon (**q**) wavevector grids. This inevitably lacks the rigor to accurately determine the mode-level e-p interactions and linewidths quantifying electronic lifetimes and mean-free paths (Λ_e) with sufficient resolution to accurately predict the thermophysical properties such as $G(T_e)$ and $\kappa_e(T_e)$. More recently, fine meshes of **q** and **k** wavevector grids have been utilized to calculate e-p coupling interactions in various metals [43–47]. However, these studies have not considered the effect of strong e-p nonequilibrium (where the electronic states are perturbed to several thousands of degrees above ambient conditions) on the e-p interactions and the resulting thermophysical and transport properties, which is what we seek to uncover through accurate calculations on dense wavevector grids in this work.

For highly nonequilibrium regimes, where the electronic temperature is elevated to the same order as the Fermi energy, finite-temperature DFT calculations have shown that the lattice dynamics in elemental metals depend on the interplay between ion-ion and ion-electron-ion interactions [48–50]. As mentioned above, this is the scenario immediately following femtosecond laser irradiation of metals, where highly nonequilibrium states of matter coexist and the interaction between these states can be drastically different as compared to scattering mechanisms dictating the e-p coupling at ambient conditions. For instance, the excitation of d-band electrons in gold weakens the electron screening, which increases the ion-ion potential and in turn causes the lattice to stiffen [48]. Even for free-electron metals with no d-band electrons (such as aluminum), the increase in electron kinetic energy has been shown to enhance the internal pressure and the result is considerable phonon hardening [50]. These variations can have major implications on the e-p interactions and the ensuing thermophysical properties of metals.

Herein, we systematically investigate the role of elevated electron temperatures and the concomitant changes on the phonon spectrum as well as the electronic DOS on the e-p interactions and the thermophysical properties of metals. For this, we consider a prototypical free-electron-like metal (aluminum), and an extensively studied noble metal (gold). More specifically, we perform density functional perturbation theory (DFPT) calculations for electronic perturbations of up to $k_B T_e = 6$ eV to show that the excitation of the electron gas can drastically decrease the overall e-p coupling in gold while it has a negligible influence on aluminum. We attribute this to the vastly different electronic structures of the two metals, where the excitation of the low-lying d bands with relatively high DOS as compared to the s bands with low DOS in gold, leads to considerable lattice stiffening and the decrease in the e-p coupling strength. We also find that the average diffusive Λ_e in gold is doubled (from ~35 nm at ambient conditions to ~70 nm at $k_B T_e = 6$ eV) as a result of e-p nonequilibrium. In comparison, the increase in the average Λ_e in aluminum is not as pronounced (increasing from ~19 nm at ambient conditions to ~23 nm at $k_B T_e = 6$ eV). The drastic increase in Λ_e for gold translates to an increase in electron thermal conductivity by more than two orders of magnitude for $T_e >$ 20000 K. For Al, the electron gas perturbation has a reduced influence on the electron thermal conductivity, which only increases by a factor of ~70 above those temperatures. Our results highlight the effects of hot electron dynamics on the thermophysical and transport properties of elemental metals, which is crucial in understanding the temporal evolution of the energy carriers when they are perturbed to several thousands of Kelvin temperature in comparison to the colder metallic lattice, a scenario commonly encountered in femtosecond laser-excited metals.

II. METHODOLOGY

We use the QUANTUM ESPRESSO package [51] to carry out our DFPT calculations. We determine the e-p matrix elements through the ELECTRON PHONON WANNIER (EPW) package. The electronic states are scattered by specific phonon modes with energy $\hbar\omega$ from one particular state to another. The likelihood of occurrence of this event is quantified by the Eliashberg coupling function, $\alpha^2 F(\omega)$. The accurate

calculation of Eliashberg function is fundamental to the accurate determination of the e-p coupling. Therefore, for the accurate calculation of Eliashberg function, dense **q** and **k** wavevector grids in the Brillouin zone are necessary. The Eliashberg function is given as [52],

$$\alpha_{\text{tr}}^2 F(\omega) = \frac{1}{N(\varepsilon_{\text{F}})} \sum_{\mathbf{q}j} \sum_{\mathbf{k}nm} \left| g_{\mathbf{k}+\mathbf{q}m,\mathbf{k}n}^{\mathbf{q}j} \right|^2 \delta(\hbar\omega - \hbar\omega_{\mathbf{q}j})$$

$$\delta(\varepsilon_{\mathbf{k}n} - \varepsilon_{\text{F}})\delta(\varepsilon_{\mathbf{k}+\mathbf{q}m} - \varepsilon_{\text{F}})\eta_{\mathbf{k}+\mathbf{q}m,\mathbf{k}n}, \quad (2)$$

where j denotes the branch index of **q**, $N(\varepsilon_F)$ signifies the DOS of electrons per spin at the Fermi level, and $g_{\mathbf{k}+\mathbf{q}m,\mathbf{k}n}^{\mathbf{q}j}$ symbolizes the e-p matrix elements that quantify the scattering of an electron at the Fermi surface from the state $|\mathbf{k}n\rangle$ to the state $|\mathbf{k}+\mathbf{q}m\rangle$. The efficiency factor,

$$\eta_{\mathbf{k}+\mathbf{q}m,\mathbf{k}n} = 1 - \frac{\mathbf{v}_{\mathbf{k}n} \cdot \mathbf{v}_{\mathbf{k}+\mathbf{q}m}}{|\mathbf{v}_{\mathbf{k}n}|^2}, \quad (3)$$

accounts for the anisotropic behavior by taking different directions of scattering into consideration. It is dependent on the electron velocity $\mathbf{v}_{\mathbf{k}n}$ and is the fundamental difference between the spectral function, $\alpha^2 F(\omega)$ and the transport spectral function defined in Eq. (2). The mass enhancement parameter (λ) gives the strength of e-p coupling factor and is given as,

$$\lambda_{(\text{tr})} = 2 \int_0^\infty \frac{\alpha_{(\text{tr})}^2 F(\omega) d\omega}{\omega}. \quad (4)$$

A precondition for precise calculation of Eq. (2) is the usage of refined **k** grid in the Brillouin zone. Interpolation of the e-p matrix elements, phonon modes, and the band energies are accomplished from an initial coarse grid of $12 \times 12 \times 12$ and $6 \times 6 \times 6$ to a uniform grid of $60 \times 60 \times 60$ and $30 \times 30 \times 30$, for electron and phonon wavevector grids, respectively. This is carried out by employing maximally localized Wannier functions from the Bloch energy bands [53]. A plane wave cutoff of 816.3 eV (60 Ry) is implemented for these calculations. We use nonrelativistic norm-conserving pseudopotentials taken from the PSlibrary [54]. The exchange-correlation energy is treated with Perdew-Zunger (PZ) functional of the local density approximation (LDA) for Al and the Perdew-Burke-Ernzerhof (PBE) functionals of the generalized gradient approximation (GGA) for Au. The $5d$, $6s$ bands with 11 electrons and the $3s$, $3p$ bands with three electrons are considered as valence electrons, for Au and Al, respectively. We use single face-centered cubic unit cells for the metals. For our calculations, we do not account for spin-orbit coupling in these metals.

The elevated temperature conditions are created by smearing the Fermi-Dirac distributions with $k_{\text{B}}T_e$ varying from 0.1 eV–6 eV. Note, this method to achieve elevated electron temperatures in first-principles calculations has been extensively used in Refs. [48–50,55–60] to predict the changes in both electronic and phononic DOS due to elevated electron temperatures. Briefly, in this approach, the finite temperatures enter through the Fermi-Dirac occupation function for the electron Kohn-Sham eigenstates and through an entropy term that is present in the free energy [61].

The compactness of interpolated fine grids of **k** and **q** points are crucial for proper convergence of the e-p coupling

coefficient. We verify the convergence as well as the accuracy of Wannier representation by confirming their localized nature. The localization of the wavevector are confirmed by the spatial decay of the Hamiltonian, dynamical and the e-p coupling matrices to zero (see Fig. S1 of the Supplemental Material [62]). The decay of these matrices endorses the usage of our calculations of the high-quality interpolations. The obtained electron Hamiltonian is given as,

$$H_{\mathbf{R}_e,\mathbf{R}'_e}^{\text{el}} = \sum_{\mathbf{k}} w_{\mathbf{k}} \mathrm{e}^{-i\mathbf{k}\cdot(\mathbf{R}'_e - \mathbf{R}_e)} U_{\mathbf{k}}^{\dagger} H_{\mathbf{k}}^{\text{el}} U_{\mathbf{k}}, \quad (5)$$

here $w_{\mathbf{k}}$ represents the weight of **k** points, $\mathbf{R}_e$ denotes the electron unit cell, and the gauge matrix $U_{\mathbf{k}}$ yields the conversion between Bloch eigenstates and the maximally localized functions. The dynamical matrix to real-space transformation is carried out using

$$D_{\mathbf{R}_p,\mathbf{R}'_p}^{\text{ph}} = \sum_{\mathbf{q}} w_{\mathbf{q}} \mathrm{e}^{-i\mathbf{q}\cdot(\mathbf{R}'_p - \mathbf{R}_p)} \mathbf{e}_{\mathbf{q}} D_{\mathbf{q}}^{\text{ph}} \mathbf{e}_{\mathbf{q}}^{\dagger}, \quad (6)$$

where $w_{\mathbf{q}}$ symbolizes the weight of the **q** points and $\mathbf{e}_{\mathbf{q}}$ represents the orthogonal eigenvalue dynamical matrix. Subsequently, the e-p matrix elements are given as,

$$g(\mathbf{R}_e, \mathbf{R}_p) = \frac{1}{N_p} \sum_{\mathbf{q},\mathbf{k}} w_{\mathbf{k}} w_{\mathbf{q}} \mathrm{e}^{-i(\mathbf{k}\cdot\mathbf{R}_e + \mathbf{q}\cdot\mathbf{R}_p)} U_{\mathbf{k}+\mathbf{q}}^{\dagger} g(\mathbf{k}, \mathbf{q}) U_{\mathbf{k}} \mathbf{u}_{\mathbf{q}}^{-1},$$
$$(7)$$

where $U_{\mathbf{k}}$ and $U_{\mathbf{k}+\mathbf{q}}$ denote electronic matrices, $\mathbf{u}_{\mathbf{q}}$ symbolizes the phonon eigenvectors scaled by atomic masses, and N_p symbolizes the number of unit cells in the period supercell [63,64]. As the distance increases, all the quantities rapidly decay to zero in the electron or phonon unit cells as shown in Fig. S1 of the Supplemental Material [62].

III. RESULTS AND DISCUSSIONS

We show the changes in the electronic DOS for Au an Al as obtained from our DFT calculations for several electron temperatures in Figs. 1(a) and 1(b), respectively. We assume that the electrons have thermalized among themselves and can be described by the Fermi-Dirac distribution for all of our calculations. This is a valid assumption for time regimes greater than the electron-electron scattering time, which is less than ∼600 fs for photoexcited gold films as determined by Fann *et al.* [36] using laser photoemission spectroscopy. With increasing electron temperature, the d bands in Au shift towards lower energies with a gradually reduced width in their energy spectrum. This excitation of d-band electrons in gold weakens the electron screening, thus increasing the effective ion-ion potential as will be discussed in more detail below [48]. In contrast, for Al, the electronic DOS remains constant over the entire temperature range. These characteristic changes in the electronic DOS for Au and Al can be further visualized in the band structure calculations as shown in Figs. 1(c) and 1(d) for Au and Al, respectively. For Au, the elevated electron temperature of 6 eV leads to the shrinking of the energy spectrum for the d bands. For Al, there is no variation in the band structure for the entire temperature perturbation range. We also plot the chemical potential for both Al and Au as a function of electron temperature as shown in Fig. 1(e). Note, we obtain the
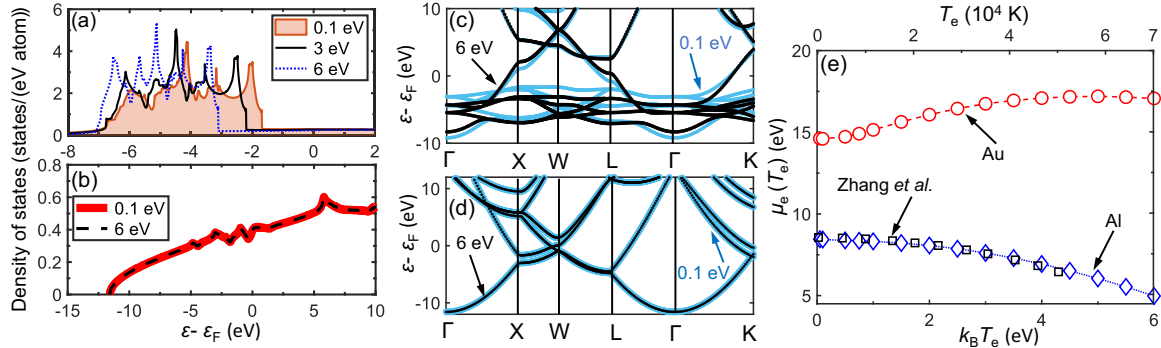
FIG. 1. Electronic density of states for (a) Au and (b) Al at varying electron temperatures as obtained from parameter-free density functional theory calculations. Electronic band structures for (c) Au and (d) Al at electron temperatures of 0.1 eV and 6 eV. (e) Variation in the chemical potential for Au and Al with increasing electron temperatures. The hollow black squares denote the finite-temperature DFT calculations of the chemical potential for Al as reported by Zhang *et al.* [55]. The agreement between our results and that of Zhang *et al.* [55] provides confidence in our results of the electronic structure calculations.

chemical potentials through our self-consistent field calculations. The chemical potential increases monotonically for Au while it decreases for Al with increasing electron temperatures. For Al, our results match well with prior calculations of Zhang *et al.* [55] that utilized similar Fermi smearing approach to perform finite-temperature DFT calculations. Their calculations utilizing the GGA matches well with our LDA-based calculations providing further confidence in our results. Taken together, the results from our electronic structure calculations that show the contrasting behaviors of the two metals under elevated electron temperatures have a significant role in dictating their vastly differing electron temperature dependencies of their thermophysical properties, as we discuss in detail below.

We plot the Fermi surfaces of Au and Al colored according to the Fermi velocities at different electron perturbations in Figs. 2(a) and 2(b), respectively. The Brillouin zones are outlined as black lines. As the Fermi surface separates the occupied from the unoccupied electronic states, the transport properties of electrons are highly dependent on where they are on the Fermi surface [65]. For Au, at low electron perturbations, the Fermi surface is nearly spherical with eight necks that touch the hexagonal faces along the ⟨111⟩ directions. At higher electron perturbations, the Fermi surface expands and the necking regions that touch the zone boundaries gradually expand. At the zone boundary, there is an energy gap associated with the Bragg reflection of electrons and consequently the energy bands flatten out as it approaches the zone edge [65]. Similarly, for Al, the Fermi surface expands and touches the hexagonal surfaces of the zone boundaries. However, unlike in Au, the Fermi velocity in Al decreases for high electron perturbations. This is quantitatively shown in Fig. 2(c) where we plot the average Fermi velocity as a function of electron perturbation energy. While the velocity increases monotonically throughout the electron temperature range for Au, the variation in velocity is negligible over the entire temperature range for Al. We will now discuss how these changes in the electronic structures of the metals affect their e-p coupling and the ensuing transport properties.

First, we consider the effect of thermal excitation of electrons on the electronic heat capacities of the metals. The temperature-dependent heat capacities of metals can be cal-

culated from the derivative of the total energy density with respect to T_e, and is given as,

$$C_e(T_e) = \int_{-\infty}^{\infty} \frac{\partial f(\varepsilon, \mu, T_e)}{\partial T_e} g(\varepsilon) \varepsilon d\varepsilon. \tag{8}$$
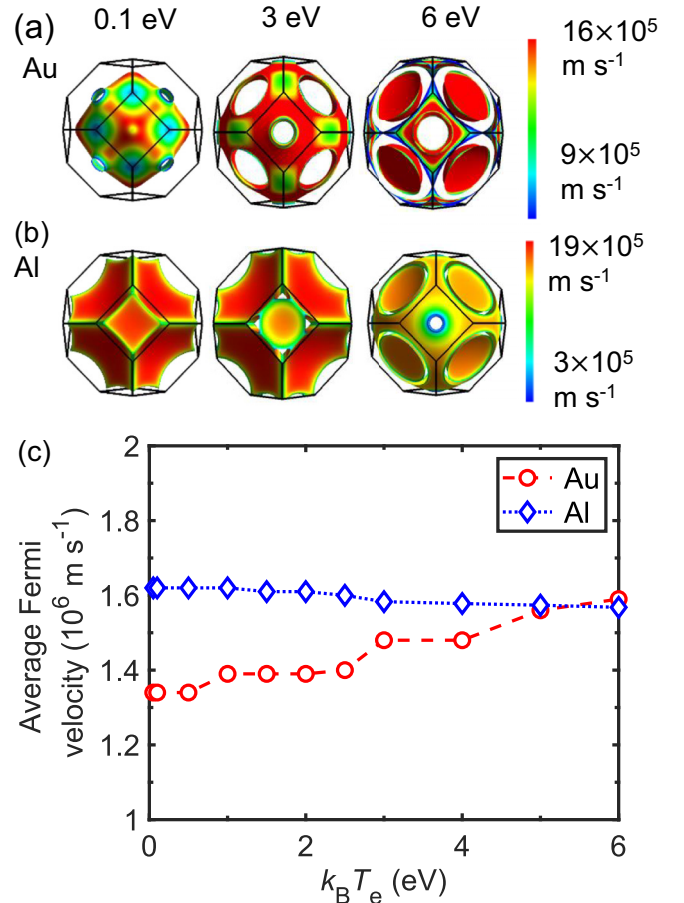

FIG. 2. Evolution of Fermi surfaces for (a) Au and (b) Al at three different electron temperatures. Color represents the variation in Fermi velocities at the Fermi surface. (c) Average Fermi velocity plotted as a function electron temperature. The Fermi velocity increases for Au while for Al, it has a slight decrease over the entire temperature range.
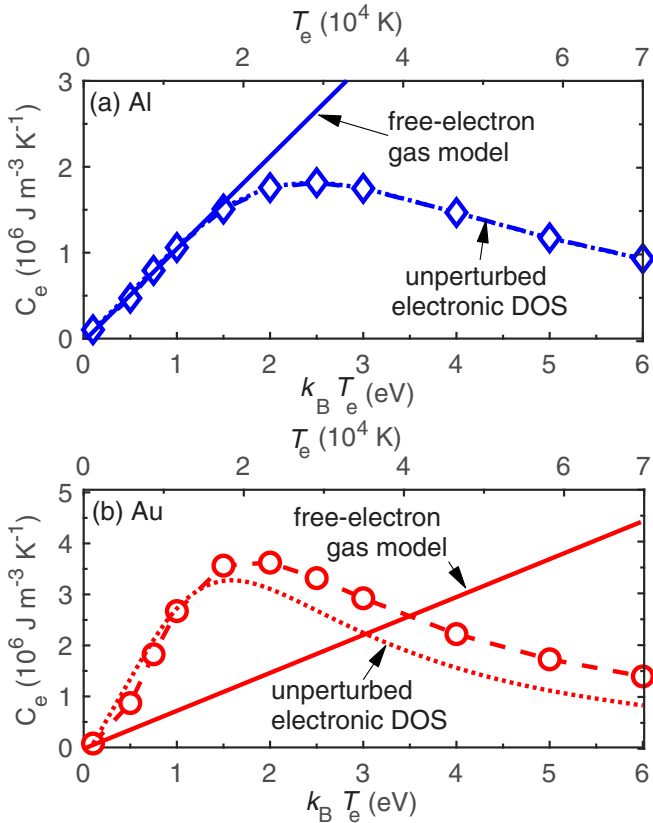
FIG. 3. Temperature-dependent heat capacities $C_e(T_e)$, calculated as a function of electron temperature, for (a) Al and (b) Au. For comparison, we also plot the predictions from the simplified free-electron model along with predictions of Eq. (9) that utilizes the unperturbed electronic density of states (calculated at $T_e = 0$ K). For Al, the free-electron gas model agrees well with our parameter-free calculations at lower temperatures, whereas it significantly underpredicts our DFT-based calculations at higher electron temperatures. For Au, the free-electron gas model can not predict the temperature dependence of the heat capacity for the entire temperature range. Furthermore, for the case of Au, the use of the unperturbed electronic density of states also leads to erroneous calculations of heat capacity, especially at higher electron temperatures.

The heat capacity depends on electronic states within a few $k_B T_e$ near ε_F since the term $\partial f / \partial T_e$ has a sharp peak at ε_F with a width of $\sim k_B T_e$. Figure 3 shows the calculations of Eq. (8), where we have utilized the electronic DOS that are calculated based on the prescribed perturbations to the electron gas. We also plot the predictions from the free-electron model for heat capacity, that utilizes the Sommerfeld expansion of the electronic free energy [30]. This formulation gives a linear temperature dependence to the heat capacity: $C_e(T_e) = \pi^2 k_B^2 n_e/3$, where n_e is the free-electron number density. As is clear, the free-electron model can only predict the heat capacity of both metals at low electron temperatures where the DOS remains free-electron-like and relatively constant near the Fermi energy. More specifically, for Al, the free-electron model predicts the heat capacity very well for lower electron temperatures of <1 eV. However, for higher electron temperatures, the free-electron model overpredicts the heat capacity for Al. For Au, the
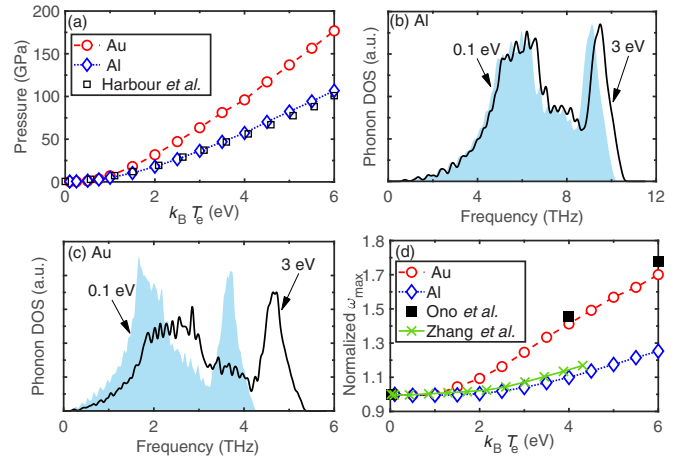

FIG. 4. (a) Comparison of electron temperature dependence of pressure in Au and Al. The hollow black squares denote variation of internal pressure with increase in electron temperature as reported by Harbour *et al.* [60]. Variations in the phonon density of states in (b) Al and (c) Au at electron temperatures of 0.1 (shaded region) and 3 eV (solid lines). (d) Variations in the maximum phonon frequency with electron temperature for Au and Al. We plot the normalized maximum frequency with respect to the maximum frequency at $k_B T_e = 0$ eV for Au and Al. The increase in pressure in Au is higher than that in Al with increasing electron temperatures, which translates to a greater phonon hardening effect in Au. We compare the normalized maximum frequencies for the metals with prior finite-temperature DFT calculations from Ono *et al.* [49] for Au and Zhang *et al.* [55] for Al.

free-electron model underpredicts the heat capacity up to electron temperatures of ~ 3 eV. For higher electron temperatures, however, the free-electron model overpredicts the heat capacity. These discrepancies in the predictions of heat capacities by the free-electron model is because of its failure to account for the changes in electronic structure at higher electron temperatures. Furthermore, we also plot the heat capacity where the unperturbed electronic structure is utilized to calculate Eq. (8) as carried out in prior works in Refs. [15,38]. It is not surprising that the heat capacity of Al agrees well with prior works, since the DOS for Al has no significant variations with electron temperature. For Au, however, since there is considerable changes in the electronic DOS due to high electron temperature perturbations, the heat capacity deviates from predictions of prior works that do not account for these changes in the electronic structure.

We now consider the effect of electron perturbation on the lattice dynamics of Au and Al. As shown in Fig. 4(a), as the electrons are perturbed to higher energies, the internal pressure starts to increase at ~ 1 eV for both metals. A larger increase in pressure is observed for Au, where at $k_B T_e = 6$ eV, the pressure in Au is $\sim 75\%$ higher than in Al. Note, this pressure increase is representative of quasiequilibrium pressures since the ion motion immediately after intense laser irradiation is negligible and the pressure builds up isochorically due to electron heating [60]. We compare the increase in internal pressure of Al with the results of finite-temperature
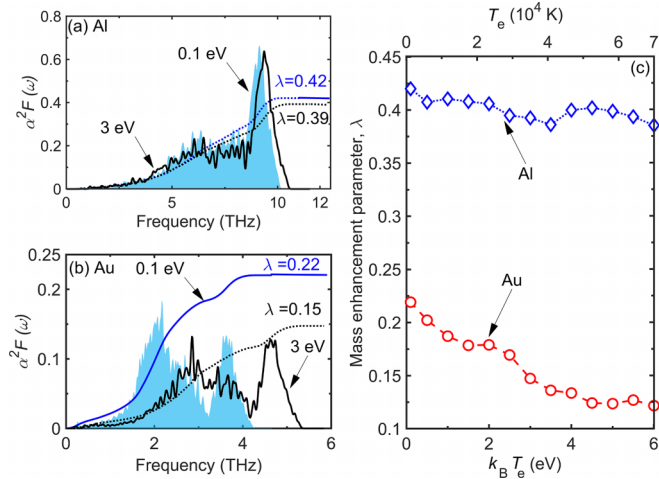
FIG. 5. (a) Eliashberg spectral functions, $\alpha^2 F(\omega)$, for (a) Al and (b) Au at electron perturbations of 0.1 and 3 eV. The solid and dotted lines represent the calculations of mass enhancement parameters (λ) at 0.1 and 3 eV, respectively. (c) Mass enhancement parameter as a function of electron temperature for the two metals.

DFT calculations that also include the molecular dynamics approach to determine the equation of state as presented in Ref. [60]. Overall, the results match well with the prior calculations providing further confidence in our calculations. For Au, the increase in the internal pressure has been ascribed to the increase in the effective ion-ion potential due to the reduced screening from exciting lower-lying electrons to higher states [48,49]. This translates to a greater stiffening of the bonds and, consequently, larger broadening in the phonon spectrum in Au as compared to Al as shown in Figs. 4(b) and 4(c), where we plot the phonon DOS of Au and Al at two different electron temperatures, respectively. The relationships between electron temperature, pressure, and phonon spectrum can be further appreciated by plotting the maximum frequency of the metals as a function of electron perturbation [Fig. 4(d)]. Similar to the change of pressure with electron temperature, the hardening of phonon modes in Au is much more pronounced than in Al. We note that the phonon hardening effect is consistent with prior results based on first-principles calculations for both Au [48,49] and Al [55], which provides confidence and validation to our results. This is demonstrated by the similar increase in maximum phonon frequencies as a function of electron temperature when compared to the DFT-based calculations by Zhang *et al.* [55] for Al and Ono *et al.* [49] for Au. Next, we will discuss the consequences of the varying responses of the lattice (due to high e-p nonequilibrium) on the e-p coupling in these two prototypical metals.

Figures 5(a) and 5(b) show our calculations of the e-p spectral (or the Eliashberg) function, $\alpha^2 F(\omega)$, at 0.1 eV and 3 eV for Al and Au, respectively. We also show the calculated values of the corresponding λ for the different electron perturbations. For the 0.1 eV temperature, our values of $\lambda = 0.42$ for Al and $\lambda = 0.22$ for Au match very well with prior DFT calculations and experimentally determined mass enhancement parameters [43,45,47]. For instance, Tong *et al.* [47] used a similar approach with the EPW package

to obtain $\lambda = 0.43$ for Al. Experimental measurements for λ have ranged from 0.38–0.48 in Al and 0.12–0.22 in Au [52], which are in excellent agreement with our calculations. Furthermore, the spectral contributions to λ at the low electron perturbation from the different phonon modes for both metals are also in agreement with prior results. The spectral function quantifies the rate of electron scattering by particular phonon modes and can lend insights into the preferential coupling of electrons to certain phonon frequencies. For Al, the peaks in $\alpha^2 F(\omega)$ only slightly shift to higher frequencies at 3 eV compared to the low perturbation case. For Au, however, the peaks shift drastically to higher frequencies along with significant decrease in the peak heights. The comparison of the Eliashberg function of the metals over the entire temperature range studied in this work are shown in Figs. S5 and S6 of the Supplemental Material [62]. Although these calculations provide spectrally resolved e-p coupling, an aggregate value of the strength of e-p coupling is represented by the e-p mass enhancement parameter, λ [66], as given by Eq. (4) and shown in Fig. 5(c) for both the metals. In contrast to Al, λ for Au decreases substantially with higher electron perturbations due to the reduction in the peak heights of the Eliashberg spectral function and the considerable stiffening of the phonon frequencies as discussed above. It is also interesting to note that a sharper decrease in λ for Au is observed at 2–2.5 eV, which is near the interband transition threshold, and highlights the significant role of excitation of the low-lying d bands on the electron dynamics in gold.

Next, we study the effect of high e-p nonequilibrium on the volumetric rate of e-p coupling, which is given as [38],

$$G = \pi \hbar k_B \lambda \langle \omega^2 \rangle \int_0^\infty \frac{(D(\varepsilon))^2}{D(\varepsilon_F)} \left[-\frac{\partial f}{\partial \varepsilon} \right] d\varepsilon, \qquad (9)$$

where $\langle \omega^2 \rangle$ is the second moment of the phonon spectrum and $D(\varepsilon)$ represents the electronic DOS [67]. Prior works have generally treated $\lambda \langle \omega^2 \rangle$ as an empirical parameter taken from low T_e thermoreflectance measurements [38,68]. However, at elevated electron temperatures, the thermal excitation of the electrons from low-lying bands below the Fermi level can significantly influence the calculations of λ, as well as perturb the phonon spectrum (and consequently $\langle \omega^2 \rangle$). Furthermore, prior works have also assumed that the electronic structure does not undergo significant changes at elevated electron temperatures [38,68]. Therefore, we compare our fully first-principles-based calculations of $G(T_e)$ with the commonly used semiempirical treatment to gauge the validity of these assumptions in Fig. 6. Not surprisingly, for Al, taking $\lambda \langle \omega^2 \rangle$ as a constant and utilizing the DOS of the unperturbed case agrees with our parameter-free predictions of $G(T_e)$. In contrast, for Au, we observe that while $G(T_e)$ at lower T_e can be well approximated by the semiempirical treatment, at elevated electron temperatures, our calculations show that $G(T_e)$ can be severely underpredicted if the correct choices for $\lambda \langle \omega^2 \rangle$ and the electronic DOS are not considered in the calculations. This shows that the conventional approach of utilizing thermodynamic properties calculated from first-principles approach without considering the elevated electron temperature effects is not suitable to predict the transport properties such as $G(T_e)$ at higher electron temperatures. This highlights the
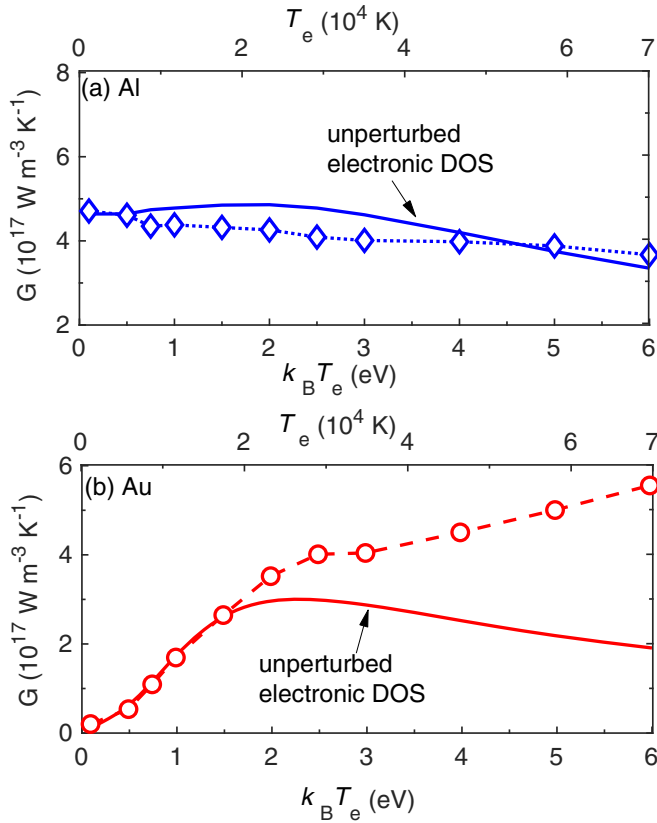
FIG. 6. Comparison of calculated volumetric electron-phonon coupling factor, $G(T_e)$, for (a) Al and (b) Au. The solid lines represent calculations of $G(T_e)$ obtained from Eq. (9) by utilizing the electronic DOS and the second moment of phonon spectrum, $\langle \omega^2 \rangle$, obtained from the calculations of the unperturbed ($T_e = 0$ K) case.

FIG. 7. Average mean-free paths, Λ_e, at the Fermi energy for Al and Au as a function of electron temperature. For Au, Λ_e increases with increase in electron temperature. However, for Al, the increase in Λ_e with electron temperature is much less pronounced, which is a direct consequence of the relatively different responses of the electron-phonon mass enhancement parameter of the two metals as shown in Fig. 5.

importance of a detailed DFPT-based calculation of the e-p coupling matrix elements and correctly accounting for effects resulting from high e-p nonequilibrium while calculating the energy exchange between hot electrons with the lattice. In this regard, we note that it is only through the recently developed Wannier interpolation technique that we have been able to perform the calculations of electron linewidths using the full formulation of the Fermi's golden rule for e-p scattering and consequently for the calculations of $G(T_e)$ for a range of electron temperatures that are carried out with dense **q** and **k** wavevector grids [44]. Note, we do not consider the temperature dependence of e-p coupling on the lattice temperature in this study. As such we only consider electronic states scattering with harmonic phonon modes.

To understand the effect of elevated electron temperatures on the characteristic scattering length scales of electrons, we plot the average mean-free path as a function of electron temperature in Fig. 7 for the two metals; we extract the energy-dependent electron lifetimes from the calculations of the e-p matrix elements and we also calculate the electron velocities to calculate our average Λ_e at the Fermi energy. Similar to the electron temperature dependence of λ, Λ_e for Al also has negligible variations with temperature. In contrast, Λ_e for Au drastically increases with electron temperature resulting from the significant weakening of the e-p coupling
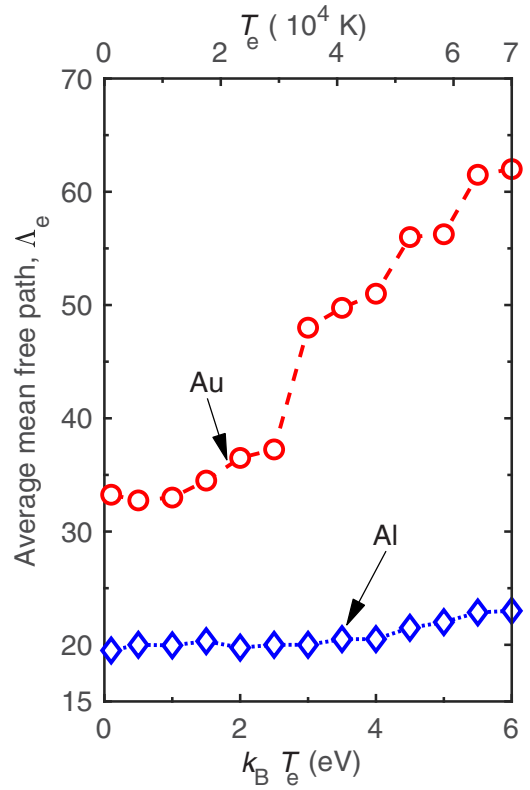
as represented by the similar decrease of λ for Au in Fig. 5(c). Moreover, similar to the sharp decrease in λ near the interband transition threshold for Au, Λ_e for Au also shows a corresponding sharp increase. We note that our calculations of the average $\Lambda_e \sim 34$ nm for Au at $k_B T_e = 0$ eV matches well with prior first-principles-based calculations [15,69].

We now consider the effect of electron temperature on the electron-driven thermal conductivities of Al and Au as shown in Figs. 8(a) and 8(b), respectively. We calculate the thermal conductivity from the Boltzmann transport equation for electrons with relaxation time approximation. The electron thermal conductivity is calculated from the sum of contributions from different electronic eigenstates as [70,71],

$$\kappa_e^{\alpha\beta} = \frac{1}{N_k} \sum_{n\mathbf{k}} c_{n\mathbf{k}} v_{n\mathbf{k}}^{\alpha} v_{n\mathbf{k}}^{\beta} \tau_{n\mathbf{k}}, \tag{10}$$

where $c_{n\mathbf{k}}$ represents the electronic heat capacity for the specific electron eigenstate, v denotes the electron group velocity, and τ is the electron relaxation time, N_k is the number of **k** points utilized in the first Brillouin zone, $n\mathbf{k}$ signifies a specific electron mode, where n is the band index, and α and β are the Cartesian coordinates. We use the electron group velocities from our DFT calculations and we obtain electron relaxation times from the calculations of the e-p coupling matrix el-
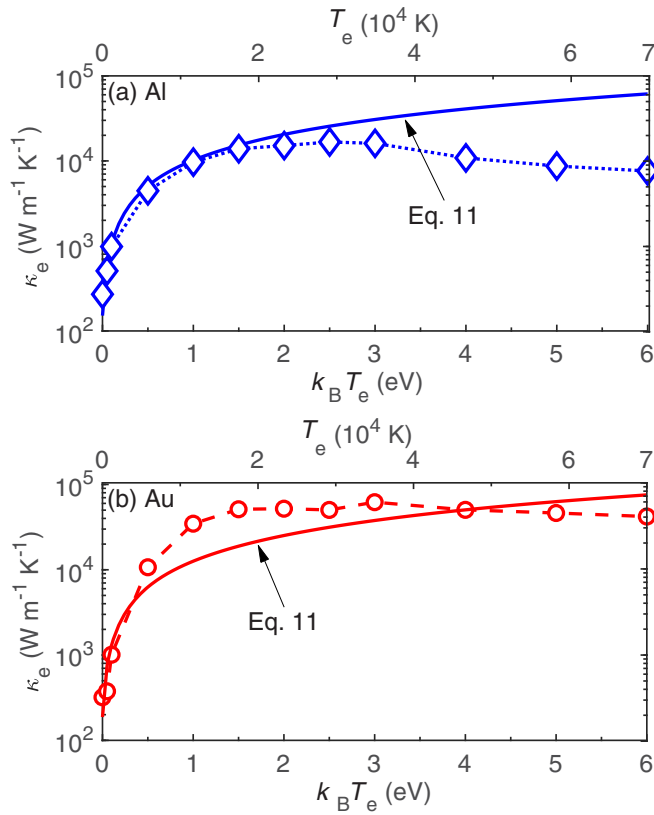
FIG. 8. (a) Electron temperature-dependent thermal conductivities, $\kappa_e(T_e)$, for (a) Al and (b) Au. The solid lines represent calculations from a simplified semiempirical model as given by Eq. (11).

ements. At 0 eV electron temperature, we predict thermal conductivities of 320 W m^{-1} K^{-1} and 270 W m^{-1} K^{-1} for Au and Al, respectively, which match well with prior theoretical and experimental values [47].

For both metals, our calculations of κ_e monotonically increase up to $T_e \sim 20000$ K, after which further increase in T_e does not lead to an any significant increase in the thermal conductivities. For comparison, we also show predictions from the simplified linear dependence on electron temperature for κ_e that is most often used in TTM calculations,

$$\kappa_e = K_0 \frac{T_e}{T_l},\qquad(11)$$

where K_0 is an empirical constant determined from low-temperature experiments [11,32,72]. This expression predicts a constant temperature-independent thermal conductivity for conditions of thermal equilibrium between the electronic gas and the lattice vibrations. However, for conditions of strong e-p nonequilibrium, depending on the metal, this simplified expression can drastically underpredict or overpredict the thermal conductivity as compared to our parameter-free DFT-based calculations. For instance, as shown in Fig. 8(a) for Al, while Eq. (11) can correctly predict the thermal conductivity for $T_e < 20000$ K, for higher T_e, our calculations deviate considerably from the linear dependence of κ_e on T_e. For Au, the decrease in the electron heat capacity beyond $T_e \sim 20000$ K is countered by the drastic increase in Λ_e along with the increase

in the Fermi velocity. Ultimately, as shown in Fig. 8(b), the thermal conductivity of gold can be increased by $\sim 200\times$ at electron temperatures of ~ 20000 K. However, for Al, the relatively insignificant increase in both the Fermi velocity and Λ_e leads to the relatively lower increase in κ_e (that only increases by $\sim 70\times$) at elevated temperatures as compared to Au.

Taken together, our parameter-free first-principles calculations have shown that, to accurately describe and analyze the hot electron dynamics in ultrafast laser-heated metals at elevated temperatures with the TTM [Eq. (1)], the proper temperature dependence of the parameters in the TTM is a prerequisite. More specifically, changes induced from the perturbed electron gas on the thermophysical properties such as $C_e(T_e)$, $G_e(T_e)$, and $\kappa_e(T_e)$ need to be accurately taken into account while analyzing the transient changes as probed by the femtosecond pump-probe experiments. These changes are particularly more significant for gold than in aluminum at elevated electron temperatures since the thermal excitation of the d bands situated ~ 2 eV below the Fermi level in gold can have drastic influence on the temperature dependence of its' thermophysical and transport properties. Therefore, utilizing semiempirical and simplified models (such as those based on the free-electron theory) in the TTM can lead to erroneous results while interpreting pump-probe experiments of laser-heated metals (see Appendix B).

IV. CONCLUSION

In conclusion, we perform first-principles calculations of e-p coupling, electronic heat capacities, mean-free paths, and thermal conductivities for a range of electron temperatures (of up to $k_B T_e = 6$ eV) for aluminum and gold. We show that the electron temperature dependence of the e-p coupling and the ensuing thermophysical properties are highly dependent on the electronic structure and its variance with temperature. For gold, we find that the mass enhancement parameter decreases substantially at elevated electron temperatures, whereas, for aluminum, it remains relatively insensitive to the electron perturbation. This results in significantly increased lifetimes and mean-free paths of electrons in gold at elevated temperatures, while the increase is not as pronounced in the case of aluminum. As such, the increase in thermal conductivity for gold is significantly higher, which increases by more than two orders of magnitude at electron temperatures above ~ 20000 K. Overall, we find that our parameter-free calculations of the thermophysical properties do not agree with the predictions from the free-electron theory based model or with a simplified model that is based on the unperturbed electronic structure of the metals. We attribute this to the substantial dependence of the electronic density of states and the electron-phonon matrix elements on the electronic temperature, which is especially important for gold where the thermal excitation of the d-band electrons can significantly influence the thermophysical properties. Our results help shed light on the hot electron dynamics in metals and has direct implications for analyzing and comprehensively understanding time-resolved pump-probe experiments on metals and metallic nanostructures.
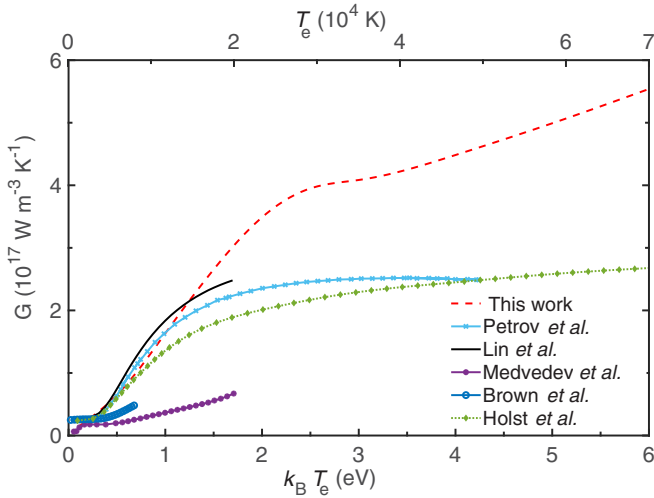
FIG. 9. Comparison of $G(T_e)$ obtained from our calculation for Au with various theoretically reported values. Theoretically reported values include those of Petrov *et al.* [73], Lin *et al.* [38], Holst *et al.* [74], Medvedev *et al.* [75], and Brown *et al.* [15].

APPENDIX A: COMPARISON OF THE VOLUMETRIC ELECTRON-PHONON COUPLING FACTOR $G(T_e)$ WITH PRIOR THEORETICAL CALCULATIONS

Here, we compare our calculations of $G(T_e)$ using Eq. (9) with predictions from prior works that have considered the temperature dependence of the e-p coupling factor. Figure 9 shows our calculations of $G(T_e)$ for Au compared to the results from prior literature. For our calculations, we have taken our fully first-principles based calculations of $\lambda\langle\omega^2\rangle$ along with the electronic DOS that vary with electron temperatures, and thus affect the calculations of $G(T_e)$. For Au, λ decreases from 0.22–0.12 as the electron temperature is increased from 0.1 eV–6 eV as shown in Fig. 5(c). Moreover there is significant shrinkage in the energy spectrum for the d bands with increasing electron temperature for Au as shown in Fig. 1(a). The second moment of phonon spectrum, $\langle\omega^2\rangle$, increases by $\sim6\times$ when the electron temperature is increased from 0.1 eV–6 eV. Therefore, we obtain a significant increase in $G(T_e)$ for Au with increasing electron temperature as shown in Fig. 9. First, we compare our results to that of Lin *et al.*'s [38] calculations, which used an unperturbed DOS and low-temperature experimental measurements for $\lambda\langle\omega^2\rangle$ to calculate $G(T_e)$. As their calculations do not account for phonon hardening effects due to excitation of electrons from low-lying d bands to higher states, which can severely affect the e-p coupling dynamics at higher temperatures (as shown in this work), our results significantly deviates from their predictions at higher electron temperatures (>20000 K). Similarly, Petrov *et al.* [73] solved the e-p Boltzmann collision integral with effective electron masses for s- and d-band electrons and applied the Lindhard screening to calculate their $G(T_e)$. In their calculations they only consider the interactions between electrons and the lon-

gitudinal acoustic phonons in Au, which might explain the lower values of $G(T_e)$ at higher electron temperatures calculated in their work as compared to our results. However, their calculations agree with the semiempirical predictions from Lin *et al.* Holst *et al.* [74] accounted for the changes in the electronic DOS, but their calculations used a constant $\lambda\langle\omega^2\rangle$ value for the entire temperature range. Therefore, their calculations match well with that of Petrov *et al.* and Lin *et al.* Our results match well with these calculations at low electron perturbations but deviate drastically at higher temperatures, which can be ascribed to the fact that the prior works do not account for both the varying electronic DOS with elevated electron temperatures and the variations in the $\lambda\langle\omega^2\rangle$.

Brown *et al.* [15] used energy-resolved e-p coupling strength from DFT calculations instead of empirical estimates of $\lambda\langle\omega^2\rangle$. However, in their model, they do not account for changes in the DOS with elevated electron temperatures [which leads to shrinking of the d bands in Au as shown in Fig. 1(a)]. This might explain the variation in our predictions as compared to the fully DFT-based calculations of Brown *et al.* as shown in Fig. 9. Medvedev *et al.* [75] calculated the electron-ion coupling by accounting for the evolution of the ions from the electron perturbations via a molecular dynamics approach to calculate $G(T_e)$ with increasing electron temperatures. Their method includes the evolution of atomic potential (and the corresponding phonon spectrum) as well as electron hopping matrix elements and predicts a slower increase of e-p coupling strength when compared with most other DFT-based predictions. This might not be surprising, since only their work does not necessitate the assumption of harmonic phonon modes since they invoke a molecular dynamics approach for calculating the evolution of the ion dynamics.

For Al, our calculations show that while λ decreases slightly [as shown in Fig. 5(c)], the electronic DOS does not change throughout the electron temperature range studied in this work. This results in a monotonic decrease of $G(T_e)$ from $\sim5 \times 10^{17}$ to $\sim3.8 \times 10^{17}$ W m^{-3} K^{-1} with increasing electron temperatures from 0.1–6 eV. We compare our results for Al to prior predictions of $G(T_e)$ using different theoretical models as shown in Fig. 10. Brown *et al.* [15] calculated $G(T_e)$ for Al using their energy-resolved e-p coupling but without considering the effects of increasing electron temperatures on their e-p coupling matrix. Waldecker *et al.* [77] and Zhang *et al.* [55] use similar methods to Brown *et al.* for predicting e-p coupling factor and report similar values for $G(T_e)$ as shown in Fig. 9. While our results agree with their results near 0 eV electron temperature, the disagreement at higher electron perturbations suggests that the simplified expression of Eq. (9) used in this work is not able to replicate the fully DFT-based calculations. However, our results for the higher electron temperatures better match the predictions from other works. For example, Lin *et al.* [38] used their empirical approach to calculate $G(T_e)$ for Al. Their calculations underpredict $G(T_e)$ by a scale of ~2 at 0 eV as compared to our results. This discrepancy has been attributed to the inconsistent adoption of the two-temperature model in the analysis of the experimental data used in Lin *et al.'s* calculations [77]. However, at higher temperatures, our calculations match well with their predictions. Petrov *et al.* [73] obtain similar results to Lin *et al.*, since they also use the experimental values for $\lambda\langle\omega^2\rangle$ in their calcu-
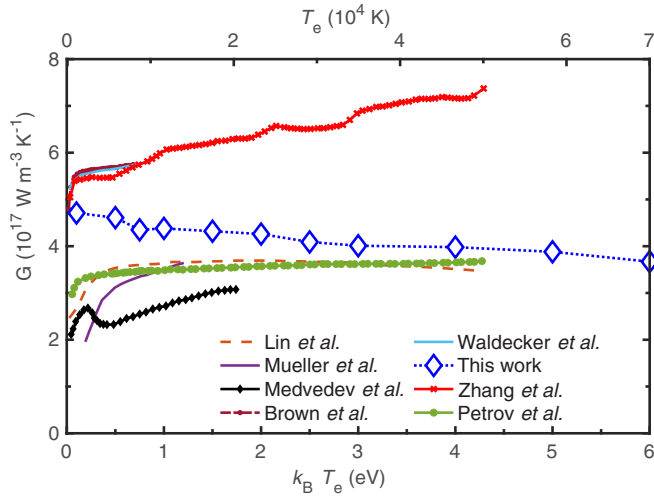
FIG. 10. Comparison of $G(T_e)$ obtained from our calculation for Al with various theoretically reported values. Theoretically reported values include those of Zhang *et al.* [55], Brown *et al.* [15], Mueller *et al.* [76], Lin *et al.* [38], Medvedev *et al.* [75], Waldecker *et al.* [77], and Petrov *et al.* [73].
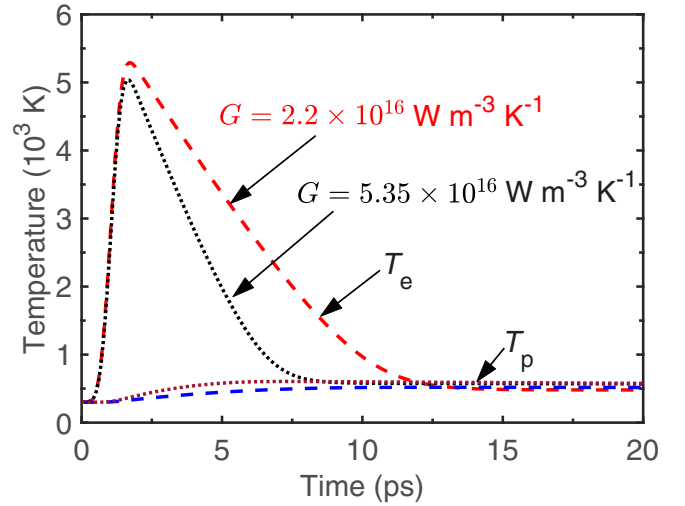

FIG. 11. Comparison of temperature profiles obtained by solving the modified TTM. The red dashed line indicates the temperature profile obtained using the room temperature e-p coupling factor of $G = 2.2 \times 10^{16}$ W m^{-3} K^{-1} and the black dotted line indicates the temperature profile obtained using the calculated e-p coupling factor of $G = 5.35 \times 10^{16}$ W m^{-3} K^{-1} at electron temperature of 0.5 eV.

lations. The electron-ion coupling calculations of Medvedev *et al.* [75] also qualitatively show an increasing trend of $G(T_e)$ with increasing electron temperature similar to that of Zhang *et al.* [55], but underpredicted by almost a factor of 2. Mueller *et al.*'s [76] use of the Boltzmann collision integral with a jellium model to define transient electron distributions in order to calculate e-p relaxation also predict a much reduced $G(T_e)$. Even though their approach considered a single-band model for calculating e-p matrix elements, their results match well with Lin *et al.*'s calculations. Taken together, these theoretical works that use different approaches (albeit based on DFT calculations) predict varying trends for $G(T_e)$ since different types of approximations have to be considered to account for the effects of the elevated electron temperature perturbations on both the electronic and lattice populations. While the closed-form analytical expression of Eq. (9) offers a simplified approach to calculate $G(T_e)$ across a wide temperature range, care must be taken while choosing the correct input parameters to be able to draw useful conclusions from the predictions. Therefore, a fully DFT-based approach that can take into account the evolution of both the changes in the electronic structure as well as account for the anharmonic lattice dynamics due to the elevated electron temperatures (without any assumptions) would be highly beneficial for understanding the evolution of $G(T_e)$ with increasing electron temperature.

APPENDIX B: INFLUENCE OF THE CHOICE OF ELECTRON-PHONON COUPLING FACTOR ON THE PREDICTIONS FROM THE TWO-TEMPERATURE MODEL

We correlate our findings with implications for femtosecond laser-based pump-probe experiments by showing the differences in electron and phonon temperature profiles obtained by solving the two-temperature model (TTM) using different values of the e-p coupling factor (G). As

we have shown in this work, at elevated electron temperatures, G is highly dependent on the temperature perturbation and can increase substantially beyond the typically accepted value of $G_0 = 2.2 \times 10^{16}$ W m^{-3} K^{-1} measured from low-temperature experiments for Au [23,78].

For pump-probe experiments, following the laser irradiation of metals, the electron and phonon temperature profiles are obtained by comparing the TTM with the thermoreflectance data [33,79]. The electron temperature (T_e) and phonon temperature (T_p) is time and space dependent and is given by Eq. (1), where $C_e(T_e) = \gamma(T_e)$, $\gamma = 71$ J m^{-3} K^{-2}, γ denotes the Sommerfield coefficient for electron heat capacity [80], $C_p = 2.45 \times 10^6$ J m^{-3} K^{-1} is representative of the phonon heat capacity [30], $\kappa_e = 317$ W m^{-1} K^{-1} represents the electron thermal conductivity [80], and $\kappa_p = 2.6$ W m^{-1} K^{-1} represents the phonon thermal conductivity [81]. The source term in the above equation is given as,

$$S(t) = \frac{0.94F(1-R)}{d(t_p + t_{ee})} exp\left(\frac{-2x^2}{r_0^2}\right)$$

$$\times exp\left[-2.77\left(\frac{t - 2(t_p + t_{ee})}{t_p + t_{ee}}\right)^2\right], \quad \text{(B1)}$$

where, F is the laser fluence incident on the surface of the gold sample, R represents the reflectivity, r_0 denotes the radius of the laser spot, d represents the film thickness, t_p symbolizes the laser spot width, and t_{ee} is the e-e thermalization time. First, we use $G = 2.2 \times 10^{16}$ W m^{-3} K^{-1} as the room temperature e-p coupling coefficient [82] to predict the temperature profiles after a typical pump-probe experiment utilizing a laser fluence of 25 J m^{-2} [7]. The predictions made by utilizing this e-p coupling constant is shown in Fig. 11. We also predict the temperature profiles by utilizing a value of $G = 5.35 \times 10^{16}$ W m^{-3} K^{-1}, which we calculate for

electron temperatures of ∼5000 K (the maximum temperature achieved in the experiment for a laser fluence of $25\,\mathrm{J\,m^{-2}}$). As shown in Fig. 11, the use of the two different G values predict completely varying temperature profiles with a faster electron temperature profile decay for the case of the higher G value. This shows that the correct choice of G is a necessary prerequisite for using the TTM to analyze the pump-probe experiments. It is also interesting to note that while the electron temperature dependence drastically changes with varying G, the lattice temperature is comparably less sensitive to this choice. This suggests that the electronic temperature is a better probe for measuring G through experiments. We note that the proper method to analyze the experimental data would be to use a temperature-dependent $G(T_e)$ for the entire pump-probe delay times to predict more accurate electron and phonon temperature profiles, which deserves further work.

[1] P. B. Allen and B. Mitrović, Theory of superconducting tc, Solid State Phys. **37**, 1 (1983).

[2] P. B. Allen, Empirical electron-phonon λ values from resistivity of cubic metallic elements, Phys. Rev. B **36**, 2920 (1987).

[3] J.-J. Zhou, J. Park, I. Timrov, A. Floris, M. Cococcioni, N. Marzari, and M. Bernardi, *Ab Initio* Electron-Phonon Interactions in Correlated Electron Systems, Phys. Rev. Lett. **127**, 126404 (2021).

[4] G. E. Bauer, E. Saitoh, and B. J. Van Wees, Spin caloritronics, Nature Mater. **11**, 391 (2012).

[5] S. Y. Savrasov, D. Y. Savrasov, and O. K. Andersen, Linear-Response Calculations of Electron-Phonon Interactions, Phys. Rev. Lett. **72**, 372 (1994).

[6] B. Liao, B. Qiu, J. Zhou, S. Huberman, K. Esfarjani, and G. Chen, Significant Reduction of Lattice Thermal Conductivity by The Electron-Phonon Interaction in Silicon with High Carrier Concentrations: A First-Principles Sstudy, Phys. Rev. Lett. **114**, 115901 (2015).

[7] A. Giri, J. T. Gaskins, B. M. Foley, R. Cheaito, and P. E. Hopkins, Experimental evidence of excited electron number density and temperature effects on electron-phonon coupling in gold films, J. Appl. Phys. **117**, 044305 (2015).

[8] W.-L. Chan, R. S. Averback, D. G. Cahill, and Y. Ashkenazy, Solidification Velocities in Deeply Undercooled Silver, Phys. Rev. Lett. **102**, 095701 (2009).

[9] W.-L. Chan, R. S. Averback, D. G. Cahill, and A. Lagoutchev, Dynamics of femtosecond laser-induced melting of silver, Phys. Rev. B **78**, 214107 (2008).

[10] W.-L. Chan, R. S. Averback, and D. Cahill, Nonlinear energy absorption of femtosecond laser pulses in noble metals, Appl. Phys. A **97**, 287 (2009).

[11] D. S. Ivanov and L. V. Zhigilei, Combined atomistic-continuum modeling of short-pulse laser melting and disintegration of metal films, Phys. Rev. B **68**, 064114 (2003).

[12] A. D. Wright, C. Verdi, R. L. Milot, G. E. Eperon, M. A. Pérez-Osorio, H. J. Snaith, F. Giustino, M. B. Johnston, and L. M. Herz, Electron–phonon coupling in hybrid lead halide perovskites, Nat. Commun **7**, 11755 (2016).

[13] D. B. Straus and C. R. Kagan, Electrons, excitons, and phonons in two-dimensional hybrid perovskites: Connecting structural, optical, and electronic properties, J. Phys. Chem. Lett. **9**, 1434 (2018).

[14] F. Thouin, D. A. Valverde-Chávez, C. Quarti, D. Cortecchia, I. Bargigia, D. Beljonne, A. Petrozza, C. Silva, and A. R. Srimath Kandada, Phonon coherences reveal the polaronic character of excitons in two-dimensional lead halide perovskites, Nature Mater. **18**, 349 (2019).

[15] A. M. Brown, R. Sundararaman, P. Narang, W. A. Goddard III, and H. A. Atwater, *Ab initio* phonon coupling and optical response of hot electrons in plasmonic metals, Phys. Rev. B **94**, 075120 (2016).

[16] A. M. Brown, R. Sundararaman, P. Narang, A. M. Schwartzberg, W. A. Goddard III, and H. A. Atwater, Experimental and *Ab Initio* Ultrafast Carrier Dynamics in Plasmonic Nanoparticles, Phys. Rev. Lett. **118**, 087401 (2017).

[17] H. A. Atwater and A. Polman, Plasmonics for improved photovoltaic devices, Nature Mater. **9**, 205 (2010).

[18] C. Clavero, Plasmon-induced hot-electron generation at nanoparticle/metal-oxide interfaces for photovoltaic and photocatalytic devices, Nature Photon. **8**, 95 (2014).

[19] M. Moskovits, The case for plasmon-derived hot carrier devices, Nature Nanotechnol. **10**, 6 (2015).

[20] S. Mukherjee, F. Libisch, N. Large, O. Neumann, L. V. Brown, J. Cheng, J. B. Lassiter, E. A. Carter, P. Nordlander, and N. J. Halas, Hot electrons do the impossible: Plasmon-induced dissociation of H_2 on Au, Nano Lett. **13**, 240 (2013).

[21] M. J. Kale, T. Avanesian, and P. Christopher, Direct photocatalysis by plasmonic nanostructures, ACS Catal. **4**, 116 (2014).

[22] P. Drude, Galvanomagn. thermomagn, Effecte **308**, 369 (1900).

[23] S. D. Brorson, A. Kazeroonian, J. S. Moodera, D. W. Face, T. K. Cheng, E. P. Ippen, M. S. Dresselhaus, and G. Dresselhaus, Femtosecond room-temperature measurement of the electron-phonon coupling constant γ in metallic superconductors, Phys. Rev. Lett. **64**, 2172 (1990).

[24] G. L. Eesley, Generation of nonequilibrium electron and lattice temperatures in copper by picosecond laser pulses, Phys. Rev. B **33**, 2144 (1986).

[25] R. W. Schoenlein, W. Z. Lin, J. G. Fujimoto, and G. L. Eesley, Femtosecond Studies of Nonequilibrium Electronic Processes in Metals, Phys. Rev. Lett. **58**, 1680 (1987).

[26] G. L. Eesley, Observation of Nonequilibrium Electron Heating in Copper, Phys. Rev. Lett. **51**, 2140 (1983).

[27] R. H. M. Groeneveld, R. Sprik, and Ad. Lagendijk, Ultrafast Relaxation of Electrons Probed by Surface Plasmons at a Thin Silver Film, Phys. Rev. Lett. **64**, 784 (1990).

[28] C. Suárez, W. E. Bron, and T. Juhasz, Dynamics and Transport of Electronic Carriers in Thin Gold Films, Phys. Rev. Lett. **75**, 4536 (1995).

[29] M. Kaganov, E. Lifshitz, and L. Tanatarov, Relaxation between electrons and the crystalline lattice, Sov. Phys. JETP **4**, 173 (1957).

[30] C. Kittel, *Introduction to Solid State Physics*, 6th ed., translated by Y, Uno, N. Tsuya, A. Morita and J. Yamashita (Maruzen, Tokyo, 1986), pp, 124.

[31] J. Chen, W. Latham, and J. Beraun, The role of electron–phonon coupling in ultrafast laser heating, J. Laser Appl. **17**, 63 (2005).

[32] J. Hohlfeld, S.-S. Wellershoff, J. Güdde, U. Conrad, V. Jähnke, and E. Matthias, Electron and lattice dynamics following optical excitation of metals, Chem. Phys. **251**, 237 (2000).

[33] P. E. Hopkins, J. C. Duda, B. Kaehr, X. Wang Zhou, C.-Y. Peter Yang, and R. E. Jones, Ultrafast and steady-state laser heating effects on electron relaxation and phonon coupling mechanisms in thin gold films, Appl. Phys. Lett. **103**, 211910 (2013).

[34] C.-K. Sun, F. Vallée, L. H. Acioli, E. P. Ippen, and J. G. Fujimoto, Femtosecond-tunable measurement of electron thermalization in gold, Phys. Rev. B **50**, 15337 (1994).

[35] P. E. Hopkins, J. L. Kassebaum, and P. M. Norris, Effects of electron scattering at metal-nonmetal interfaces on electron-phonon equilibration in gold films, J. Appl. Phys. **105**, 023710 (2009).

[36] W. S. Fann, R. Storz, H. W. K. Tom, and J. Bokor, Direct Measurement of Nonequilibrium Electron-Energy Distributions in Subpicosecond Laser-Heated Gold Films, Phys. Rev. Lett. **68**, 2834 (1992).

[37] P. E. Hopkins, Multiple phonon processes contributing to inelastic scattering during thermal boundary conductance at solid interfaces, J. Appl. Phys. **106**, 013528 (2009).

[38] Z. Lin, L. V. Zhigilei, and V. Celli, Electron-phonon coupling and electron heat capacity of metals under conditions of strong electron-phonon nonequilibrium, Phys. Rev. B **77**, 075133 (2008).

[39] A. Giri and P. E. Hopkins, Transient thermal and nonthermal electron and phonon relaxation after short-pulsed laser heating of metals, J. Appl. Phys. **118**, 215101 (2015).

[40] Z. Lin and L. V. Zhigilei, Temperature dependences of the electron–phonon coupling, electron heat capacity and thermal conductivity in ni under femtosecond laser irradiation, Appl. Surf. Sci. **253**, 6295 (2007).

[41] S. Y. Savrasov and D. Y. Savrasov, Electron-phonon interactions and related physical properties of metals from linear-response theory, Phys. Rev. B **54**, 16487 (1996).

[42] R. Bauer, A. Schmid, P. Pavone, and D. Strauch, Electron-phonon coupling in the metallic elements al, au, na, and nb: A first-principles study, Phys. Rev. B **57**, 11276 (1998).

[43] A. Giri, J. T. Gaskins, L. Li, Y.-S. Wang, O. V. Prezhdo, and P. E. Hopkins, First-principles determination of the ultrahigh electrical and thermal conductivity in free-electron metals via pressure tuning the electron-phonon coupling factor, Phys. Rev. B **99**, 165139 (2019).

[44] S. Poncé, E. R. Margine, C. Verdi, and F. Giustino, Epw: Electron–phonon coupling, transport and superconducting properties using maximally localized wannier functions, Comput. Phys. Commun. **209**, 116 (2016).

[45] A. Jain and A. J. H. McGaughey, Thermal transport by phonons and electrons in aluminum, silver, and gold from first principles, Phys. Rev. B **93**, 081206(R) (2016).

[46] A. Giri, M. V. Tokina, O. V. Prezhdo, and P. E. Hopkins, Electron–phonon coupling and related transport properties of metals and intermetallic alloys from first principles, Mater. Today Phys. **12**, 100175 (2020).

[47] Z. Tong, S. Li, X. Ruan, and H. Bao, Comprehensive first-principles analysis of phonon thermal conductivity and electron-phonon coupling in different metals, Phys. Rev. B **100**, 144306 (2019).

[48] V. Recoules, J. Clérouin, G. Zérah, P. M. Anglade, and S. Mazevet, Effect of Intense Laser Irradiation on the Lattice Stability of Semiconductors and Metals, Phys. Rev. Lett. **96**, 055503 (2006).

[49] S. Ono and D. Kobayashi, Lattice stability of ordered au-cu alloys in the warm dense matter regime, Phys. Rev. B **103**, 094114 (2021).

[50] F. Bottin and G. Zérah, Formation enthalpies of monovacancies in aluminum and gold under the condition of intense laser irradiation, Phys. Rev. B **75**, 174114 (2007).

[51] P. Giannozzi, S. Baroni, N. Bonini, M. Calandra, R. Car, C. Cavazzoni, D. Ceresoli, G. L. Chiarotti, M. Cococcioni, I. Dabo *et al.*, Quantum espresso: A modular and open-source software project for quantum simulations of materials, J. Phys.: Condens. Matter **21**, 395502 (2009).

[52] G. Grimvall, The electron-phonon interaction in normal metals, Phys. Scr. **14**, 63 (1976).

[53] N. Marzari, A. A. Mostofi, J. R. Yates, I. Souza, and D. Vanderbilt, Maximally localized wannier functions: Theory and applications, Rev. Mod. Phys. **84**, 1419 (2012).

[54] A. Dal Corso, Pseudopotentials periodic table: From H to Pu, Comput. Mater. Sci. **95**, 337 (2014).

[55] J. Zhang, R. Qin, W. Zhu, and J. Vorberger, Energy relaxation and electron–phonon coupling in laser-excited metals, Materials **15**, 1902 (2022).

[56] S. Ono, Lattice dynamics for isochorically heated metals: A model study, J. Appl. Phys. **126**, 075113 (2019).

[57] F. C. Kabeer, E. S. Zijlstra, and M. E. Garcia, Road of warm dense noble metals to the plasma state: *Ab initio* theory of the ultrafast structural dynamics in warm dense matter, Phys. Rev. B **89**, 100301(R) (2014).

[58] D. V. Minakov and P. R. Levashov, Melting curves of metals with excited electrons in the quasiharmonic approximation, Phys. Rev. B **92**, 224102 (2015).

[59] G.-Q. Yan, X.-L. Cheng, H. Zhang, Z.-Y. Zhu, and D.-H. Ren, Different effects of electronic excitation on metals and semiconductors, Phys. Rev. B **93**, 214302 (2016).

[60] L. Harbour, M. W. C. Dharma-wardana, D. D. Klug, and L. J. Lewis, Equation of state, phonons, and lattice stability of ultrafast warm dense matter, Phys. Rev. E **95**, 043201 (2017).

[61] N. D. Mermin, Thermal properties of the inhomogeneous electron gas, Phys. Rev. **137**, A1441 (1965).

[62] See Supplemental Material at http://link.aps.org/supplemental/10.1103/PhysRevB.107.094301 for convergence calculations for the electron-phonon mass enhancement parameters, calculations of the Fermi velocities, Eliashberg spectral functions, and electron-phonon scattering lifetimes for the entire electron temperature perturbation range.

[63] J. D. Noffsinger, Ph.D. thesis, The electron-phonon interaction from first principles, UC Berkeley, 2011.

[64] F. Giustino, M. L. Cohen, and S. G. Louie, Electron-phonon interaction using wannier functions, Phys. Rev. B **76**, 165108 (2007).

[65] S. B. Dugdale, Life on the edge: A beginner's guide to the fermi surface, Phys. Scr. **91**, 053009 (2016).

[66] P. B. Allen, Theory of thermal relaxation of electrons in metals, Phys. Rev. Lett. **59**, 1460 (1987).

[67] W. McMillan, Transition Temperature of Strong-Coupled Superconductors, Phys. Rev. **167**, 331 (1968).

[68] Z. Lin and L. V. Zhigilei, Thermal Excitation of D Band Electrons in Au: Implications for Laser-Induced Phase Transformations, in *High-Power Laser Ablation VI*, Vol. 6261 (SPIE, Bellingham, 2006), pp. 248–261.

[69] D. Gall, Electron mean free path in elemental metals, J. Appl. Phys. **119**, 085101 (2016).

[70] G. Chen, *Nanoscale Energy Transport and Conversion: A Parallel Treatment of Electrons, Molecules, Phonons, and Photons* (Oxford University Press, Oxford, 2005).

[71] T. M. Tritt, *Thermal Conductivity: Theory, Properties, and Applications* (Springer Science & Business Media, Berlin, 2005).

[72] S. S. Wellershoff, J. Gudde, J. Hohlfeld, J. G. Muller, and E. Matthias, Role of electron-phonon coupling in femtosecond laser damage of metals, in *High-Power Laser Ablation*, Vol. 3343 (SPIE, Bellingham, 1998), pp. 378–387.

[73] Y. V. Petrov, N. Inogamov, and K. P. Migdal, Thermal conductivity and the electron-ion heat transfer coefficient in condensed media with a strongly excited electron subsystem, JETP Lett. **97**, 20 (2013).

[74] B. Holst, V. Recoules, S. Mazevet, M. Torrent, A. Ng, Z. Chen, S. E. Kirkwood, V. Sametoglu, M. Reid, and Y. Y. Tsui, *Ab initio* model of optical properties of two-temperature warm dense matter, Phys. Rev. B **90**, 035121 (2014).

[75] N. Medvedev and I. Milov, Electron-phonon coupling in metals at high electronic temperatures, Phys. Rev. B **102**, 064302 (2020).

[76] B. Y. Mueller and B. Rethfeld, Relaxation dynamics in laser-excited metals under nonequilibrium conditions, Phys. Rev. B **87**, 035139 (2013).

[77] L. Waldecker, R. Bertoni, R. Ernstorfer, and J. Vorberger, Electron-Phonon Coupling and Energy Flow in a Simple Metal Beyond the Two-Temperature Approximation, Phys. Rev. X **6**, 021003 (2016).

[78] R. H. M. Groeneveld, R. Sprik, and A. Lagendijk, Femtosecond spectroscopy of electron-electron and electron-phonon energy relaxation in ag and au, Phys. Rev. B **51**, 11433 (1995).

[79] P. E. Hopkins, L. M. Phinney, and J. R. Serrano, Re-examining electron-fermi relaxation in gold films with a nonlinear thermoreflectance model, J. Heat Transfer **133**, 044505 (2011).

[80] M. Bonn, D. N. Denzler, S. Funk, M. Wolf, S.-S. Wellershoff, and J. Hohlfeld, Ultrafast electron dynamics at metal surfaces: Competition between electron-phonon coupling and hot-electron transport, Phys. Rev. B **61**, 1101 (2000).

[81] Y. Wang, Z. Lu, and X. Ruan, First principles calculation of lattice thermal conductivity of metals considering phonon-phonon and phonon-electron scattering, J. Appl. Phys. **119**, 225109 (2016).

[82] J. B. Lee, K. Kang, and S. H. Lee, Comparison of theoretical models of electron-phonon coupling in thin gold films irradiated by femtosecond pulse lasers, Mater. Trans. **52**, 547 (2011).